Influence of street trees on turbulent fluctuations and transport processes in an urban canyon: a wind tunnel study

Annika Vittoria del Ponte, Sofia Fellini, Massimo Marro, Maarten van Reeuwijk, Luca Ridolfi, Pietro Salizzoni

Influence of street trees on turbulent fluctuations and transport processes in an urban canyon: a wind tunnel study

January 21st, 2024

Annika Vittoria Del Ponte[1,2], Sofia Fellini[1,2], Massimo Marro[2], Maarten van Reeuwijk[3], Luca Ridolfi[1], Pietro Salizzoni[1,2]
[1] Department of Environmental, Land, and Infrastructure Engineering, Politecnico di Torino, Corso Duca degli Abruzzi 24, 10129 Turin, Italy
[2] Univ Lyon, Ecole Centrale de Lyon, CNRS, Univ Claude Bernard Lyon 1, INSA Lyon, LMFA, UMR5509, 69130, Ecully France
[3]Imperial College London, Department of Civil and Environmental Engineering, SW7 2AZ, London, United Kingdom

Abstract

The presence of vegetation within urban canyons leads to non-trivial patterns of the concentration of airborne pollutants, as a result of the complex structure of the velocity field. To investigate the relationship between concentration, velocity fields and vegetation density, we have performed wind-tunnel experiments in a reduced-scale street canyon, oriented perpendicular to the external wind flow, within which we placed a steady ground-level line source of a passive tracer. The aerodynamic behavior of vegetation was reproduced by inserting plastic miniatures of trees along the two long sides of the canyon, according to three different densities. The canyon ventilation was investigated by acquiring one-point simultaneous statistics of concentration and velocity over a dense grid of points within the canyon. The results show that the presence of trees hinders the upward mean vertical velocity at the rooftop, causes a reduction of the turbulent kinetic energy inside the canyon, and reduces the energy content of the large scales. The scalar concentration is conversely characterized by an enhanced level of turbulent fluctuations, whose magnitude is not dampened increasing the tree density. Within the canyon, high tree density

inhibits turbulent mass fluxes, which are instead enhanced at roof level, where the mean component of the scalar flux is however hindered. A statistical analysis of concentration time series reveals that the lognormal distribution is suitable to model concentration fluctuations and extreme events, in dispersing plumes emitted by a linear source.

1 Introduction

Inserting vegetation in the urban environment is a promising strategy to mitigate the urban heat island effect and to reduce flood risks and air pollution levels (Ferrini et al., 2020). The presence of trees in cities guarantees shading and evapotranspiration, which are fundamental for temperature regulation (Oliveira et al., 2011; Grilo et al., 2020). Green areas increase the amount of permeable surface and therefore the infiltration capacity of urban terrain. This ensures the regulation of stormwater runoff, and an increase of soil moisture for evapotranspiration (Armson et al., 2013; Zölch et al., 2017). Thanks to the large surface area of the leaves, tree crowns act as sinks of pollutants as they promote dry deposition and absorption (Hewitt et al., 2020; Diener and Mudu, 2021). Moreover, during the daytime, photosynthesis guarantees CO_2 sequestration (Nowak and Crane, 2002; Ferrini and Fini, 2011). Besides, green areas offer human and ecosystem well-being, providing natural areas for amusement, increasing biodiversity, and attenuating noise pollution (Van Renterghem et al., 2015).

However, urban vegetation may also have adverse effects on street ventilation and air quality. Notably, vegetation alters pollutant dispersion mechanisms, depending on its density, its spatial configuration, as well as the relative location of the pollutant source (Abhijith et al., 2017). Recently, Grylls and van Reeuwijk (2022) employed Large Eddy Simulations (LES) to study the effects of trees on air quality in street canyons, using a vegetation model that incorporates deposition, shading, and aerodynamic drag (Grylls and van Reeuwijk, 2021) and analysing the two competing processes affecting air quality: the beneficial role of deposition on the leaves and the reduced ventilation induced by trees aerodynamics.

Experimentally, the aerodynamic effect of vegetation on pollutant dispersion in urban areas was studied in wind tunnels, as recently reviewed by Zhao et al. (2023), laying reduced-scale vegetation in model street canyons. Gromke and Ruck (2007) performed concentration measurements in an isolated street canyon, oriented perpendicular to the wind flow, with a row of model trees placed along the central axis. They found that the presence of trees causes an increase of the mean pollutant concentration close to the upwind building and a decrease in it close to the downwind building. These effects are more pronounced with greater tree crown diameter or smaller tree spacing, whereas the crown porosity causes remarkable concentration

variations only if it is greater than 97% (Gromke and Ruck, 2009). With a wind blowing with an angle of 45° with respect to the canyon axis, the increase of pollutant concentration due to the presence of trees is still detectable, but not when the wind flow is parallel to the canyon axis (Gromke and Ruck, 2012). A vegetation-induced increase of the mean concentration within urban canyons was also observed with Reynolds-averaged Navier–Stokes simulations (Gromke et al., 2008; Buccolieri et al., 2009) and LES (Moonen et al., 2013; Merlier et al., 2018). In a recent work, Fellini et al. (2022) presented the results of an experimental campaign aimed at providing a high-resolution three-dimensional characterization of the mean scalar concentration field inside a vegetated street canyon, perpendicular to the wind flow. They found that different spatial patterns of the mean concentration emerge depending on the tree density. Moreover, the presence of trees increases the pollutant concentration at the upwind wall, mostly at the pedestrian level, even if it does not affect significantly the average concentration calculated over the whole canyon. All papers cited above focused on the spatial distribution of the time-averaged concentration within street canyons. In the present work, we aim at extending this investigation to the estimation of the turbulent mass fluxes, within the canyon, which drive the transfer of pollutant towards the external atmosphere.

The issue of the turbulent (mass and momentum) transfer between the external flow and a plant (Raupach et al., 1996; Finnigan, 2000) or urban (Garbero et al., 2010; Neophytou et al., 2014; Perret et al., 2019) canopy has been so far addressed by a large number of authors. On one side, studies on plant canopies were conducted adopting idealised (Raupach et al., 1986; Poggi et al., 2006) or (more rarely) realistic (Pietri et al., 2009) modeled trees, focusing on the role of vegetation density (Poggi et al., 2004) and terrain morphology (Poggi and Katul, 2007a,b). On the other side, most studies on the urban canopy considered simplified urban geometries, focusing on the effect of the canyon height-to-width ratio (H/W_c, where H is the height of the canyon and W_c is its width) (Di Bernardino et al., 2015, 2018; Jaroslawski et al., 2020), upstream turbulence (Salizzoni et al., 2011; Blackman et al., 2015, 2018) and thermal fluxes (Marucci and Carpentieri, 2019; Fellini et al., 2020) on the street canyon ventilation.

Studies focusing on the combined effect of both trees and building density on turbulence dynamics are however still missing. This study is a first step, forward to fill this gap. After describing the wind tunnel facility (section 2) and the measurement techniques (section 3), in section 4, we present flow (subsection 4.1) and concentration fields (subsection 4.2) and of the vertical mass fluxes (subsection 4.3), within and above the street canyon. In section 4.2.1 we provide a probabilistic characterization of concentration fluctuations, with a focus on extreme values, which have important applications in toxic risk analysis. Conclusions are drawn in section 5.

2 Experimental setup

The experimental campaign was carried out in the atmospheric wind tunnel of the Laboratoire de Mecanique des Fluides et d'Acoustique (LMFA), at the École Centrale de Lyon. It is a recirculating system, with a test section 12 m long, 2 m high and 3.5 m wide. Inside the test section, an urban street network in scale 1:200, with a geometry similar to the one adopted by Garbero et al. (2010), was created using model buildings 0.1 m high, spaced by 0.2 m in the streamwise direction and by 0.1 m in the spanwise direction (Fig. 1a). Narrower streamwise streets (H/W_n=1) and wider perpendicular streets (H/W_w=0.5) were arranged to avoid flow channeling. The roughness of the roofs was reproduced with 5 mm high steel nuts, randomly placed on the top of the blocks. A wind flow was generated by an axial fan, installed in the upper conduit of the recirculating wind tunnel. The turbulent flow was developed placing a homogeneous turbulent grid and a row of 7 Irwin spires, 0.95 m high, at the entrance of the test section. The interaction of the wind flow with the grid, the spires and the rough blocks on the floor generates a neutrally stratified boundary layer of depth δ=1.1m, with a free-stream velocity $U_\infty = \overline{u}(z = \delta)$=5m/s, where $\overline{u}$ is the mean streamwise velocity. The Reynolds number of the flow is $Re = \delta U_\infty/\nu \simeq 3.6 \times 10^5$, where $\nu \simeq 1.52 \times 10^{-5}$ m^2/s is the kinematic viscosity of the air at 19°C, which guarantees Reynolds independent flow dynamics (Allegrini et al., 2013; Marucci and Carpentieri, 2019). In the lower part of this boundary layer, in the so-called inertial layer, the mean velocity profile is well fitted by a logarithmic profile of the form

$$\overline{u}(z) = \frac{u_*}{\kappa} \ln\Big(\frac{z-d}{z_0}\Big), \tag{1}$$

where u_*=0.29 m/s is the friction velocity, κ=0.4 is the von Kármán constant, d=0.094 m is the zero-plane displacement, and $z_0 = 1 \times 10^{-3}$ m is the aerodynamic roughness length. We defined the inertial region isolating the fraction of the mean velocity profile that lays on a straight line in the semi-logarithmic plot. To obtain a precise delimitation of the inertial zone, we explored different extensions of the linear region above the roughness sub-layer in the range $0.15 < z/\delta < 0.4$ (Fellini et al., 2022). We selected u_*, d and z_0 so as to minimize the sum of the square difference between the logarithmic law (equation 1) and the velocity measurements in the linear region (Salizzoni et al., 2008). Furthermore, we verified that u_* is consistent with the value of Reynolds stresses according to the relation $u_*^2 = -\overline{u'w'}$ (Fig. 2b). In Fig. 2a, we report vertical profiles of $\overline{u}$ measured at four different positions around a building-like-obstacles – above the rooftop, above a streamwise street, above a spanwise street, and above a street intersection – and at different streamwise distances from the entrance of the test section. The vertical profiles collapse onto a single curve, meaning that the external boundary layer has reached

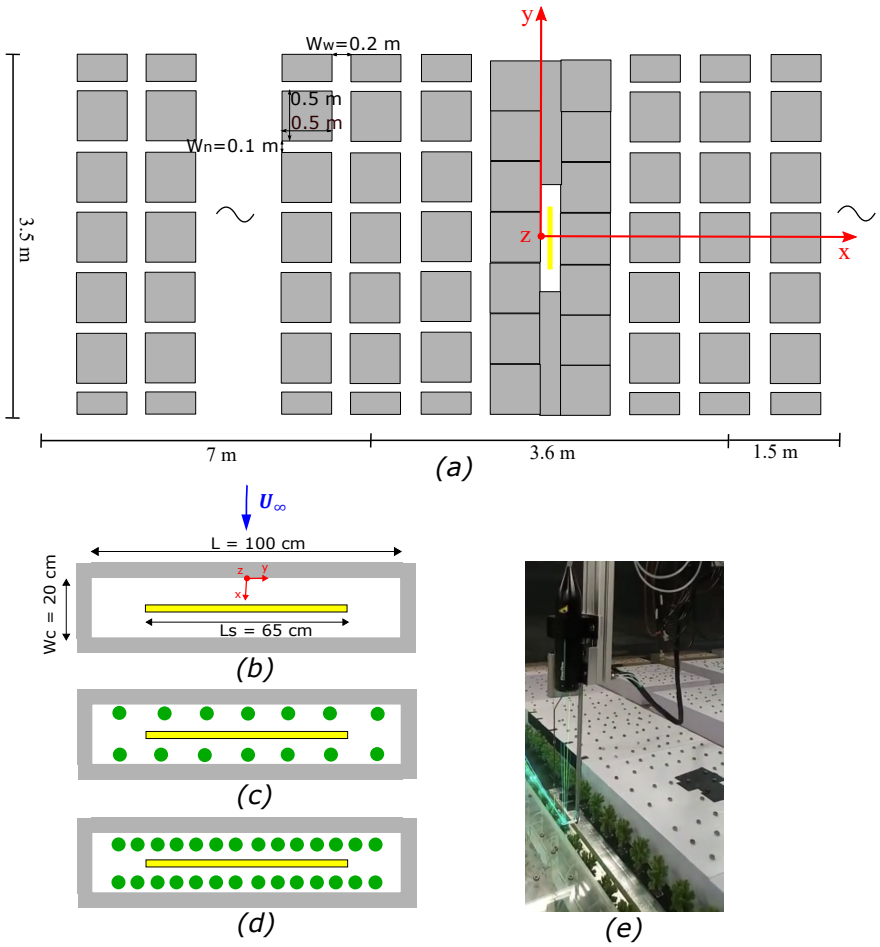

Figure 1: (a) Scheme of the urban network reproduced inside the test section of the wind tunnel. (b) Reference street canyon in the Zero (b), Half (c), and Full (d) configurations. The yellow line represents the linear source, while the green dots are the model trees. (e) System LDA-FID coupled with the mirror.

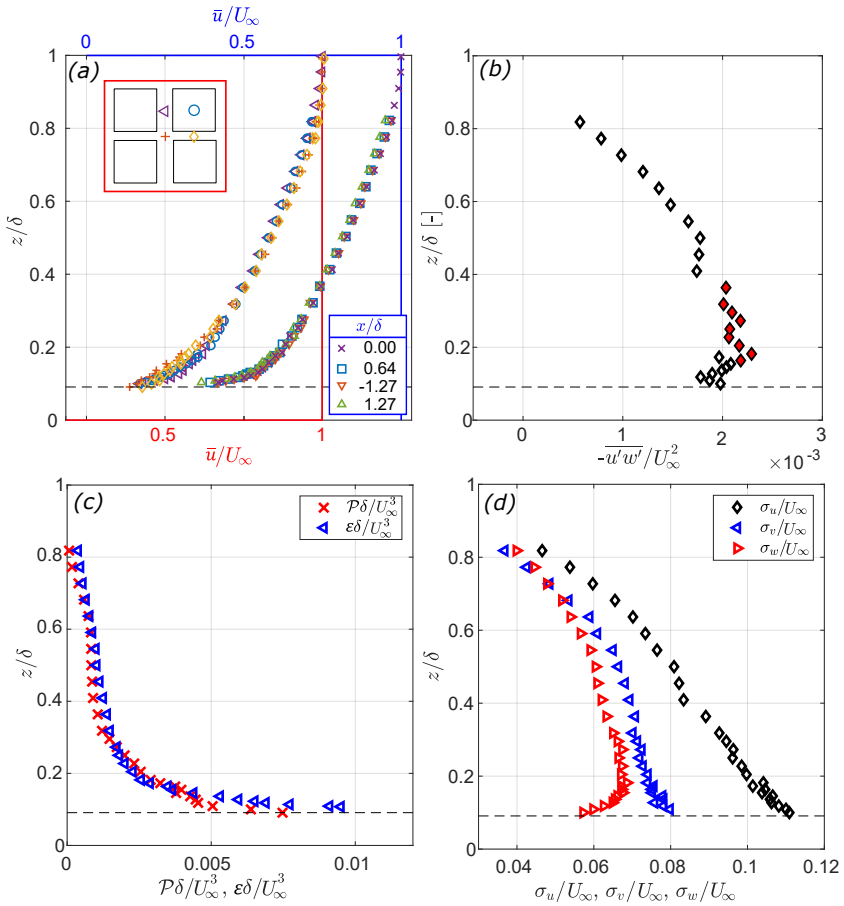

Figure 2: (a) Streamwise mean velocity profiles at the top of the building-like obstacles (black dashed line), measured at 4 different positions around a building-like-obstacle (red bottom x-axis) and at 4 different distances along the streamwise direction of the wind tunnel (blue top x-axis). (b) Reynolds stresses. The full markers represent the constant-stress region. (c) Production and dissipation rate of turbulent kinetic energy. (d) Standard deviation of the three velocity components.

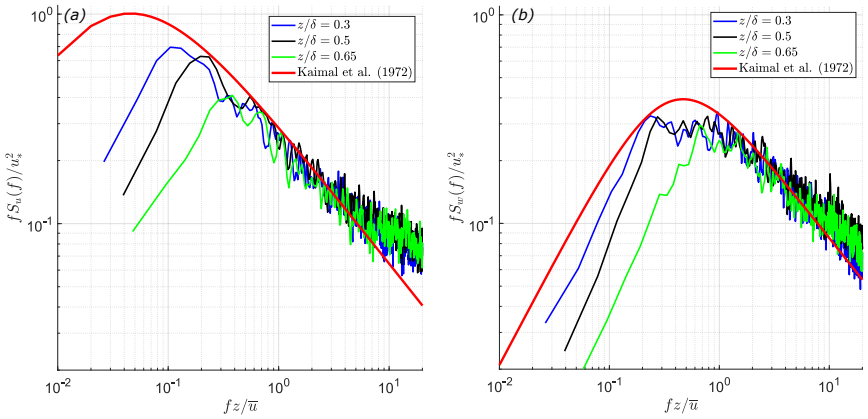

Figure 3: Velocity spectra of the streamwise velocity (a) and of the vertical velocity (b) for growing distances from the obstacles, z/δ. The empirical spectra $S_u(f)$ and $S_w(f)$ are compared with a model extrapolated from field data (Kaimal et al., 1972), represented with the red line.

an equilibrium condition. Consistently, the Reynolds stress profile clearly exhibits a constant stress region in the lower part of the velocity field (Fig. 2b) and production ($\mathcal{P}$) and dissipation (ε) of turbulent kinetic energy overlap throughout the whole boundary layer (Fig. 2c). The profiles of the standard deviation of the streamwise, transversal, and vertical velocity components (defined in Fig. 2d as σ_u, σ_v, and σ_w, respectively) show typical shapes of a neutral boundary layer (Raupach et al., 1991; Salizzoni et al., 2008; Garbero et al., 2010). Finally, we report the spectra of the streamwise velocity signal ($u(t)$) and of the vertical velocity signal ($w(t)$) for increasing distances from the obstacles (see Fig. 3). We compare them to the model proposed by Kaimal et al. (1972), based on the Kansas field experiments:

$$\frac{fS_u(f)}{u_*^2} = \frac{105n}{(1+33n)^{5/3}} \tag{2}$$

$$\frac{fS_w(f)}{u_*^2} = \frac{2n}{1+5.3n^{5/3}} \tag{3}$$

where f is the constant sampling frequency, $S_u(f)$ and $S_w(f)$ are the spectra of $u(t)$ and $w(t)$, respectively, $n = fz/\overline{u}$ in the non-dimensional frequency, z is the vertical distance, and $\overline{u}$ is the local mean longitudinal velocity. The measured spectra show a good agreement with the Kaimal's model in the inertial region, meaning that the empirical spectra are similar to atmospheric spectra. Further details on the experimental facility and on the evaluation of the boundary layer parameters, ε, and $\mathcal{P}$ are available in Fellini et al. (2022).

The reference street canyon is a closed cavity L=1m long, H=0.1m high, W_c=0.2m wide, within which the scalar ground-level line source is placed. We adopted a

canyon with lateral edges bordered by walls in order to avoid lateral mass fluxes and to define a control volume for the rigorous estimation of the ventilation efficiency, performing a mass balance between the mass flux emitted by the line source and the mass flux leaving the canyon at the rooftop. The geometry of the street canyon provides an aspect ratio H/W_c=0.5 and a length to height ratio L/H=10, which approximates the characteristics of an indefinitely long canyon (Salizzoni et al., 2009; Allegrini et al., 2013). The canyon is around 9 m away from the entrance of the test section, and it is oriented perpendicular to the wind flow direction. The ground-level linear source (simulating traffic pollutant emissions) is L_s=0.65 m long, thus it does not cover the entire length of the canyon (see yellow line in Fig. 1b), in order to avoid wall effects. It consists of a metallic tube pierced with needles emitting an ethane-air mixture within a homogenization chamber, located in a slot cut in the floor of the wind tunnel. From this chamber, the gas mixture is injected in the canyon, at ground level, through a metallic grid 65cm long and 1cm wide. The small holes of the grid produce substantial pressure drop thus rendering the gas flow in the street canyon insensitive to local pressure fluctuations. The injection flow rate is 0.4 l/min, allowing an emission velocity (equal to 0.01 m/s) sufficiently low to avoid flow perturbation in the cavity (Marro et al., 2020). Ethane was chosen as a passive tracer since it has a density similar to air. The origin of the reference system was assumed in the middle of the street canyon, at the upwind wall (see red arrows in Fig. 1a,b), with the x-coordinate oriented in the streamwise direction, the y-coordinate oriented along the canyon axis and the z-coordinate oriented upward.

The urban vegetation was simulated through plastic miniatures of trees, with a trunk of 2 cm and a porous crown, made of plastic filaments, 6.5 cm high and 4.5 cm wide. In a 1:200 scale, the miniatures represent trees 16m high and 9m wide, similar to plane trees or hypochestnuts, typically planted in tree-lined boulevards located in urban canyons flanked by buildings 20m high. The aerodynamic behavior of the model trees was characterized measuring their aerodynamic porosity and drag coefficient (Fellini et al., 2022). The aerodynamic porosity is the ratio between the spatial average wind speed downstream the obstacle and the average speed of the approaching wind. It was evaluated performing velocity measurements on a dense grid upstream and downstream a single tree, placed in a homogeneous flow. The velocity field was integrated over the tree silhouette, obtaining an aerodynamic porosity equal to 0.3, which approximates the porosity of a real tree (Manickathan et al., 2018) and is consistent with the value of the optical porosity computed with image processing. The drag coefficient was estimated as $2F/\rho_a U_{ref}^2 A_c$, where F is the drag force measured by means of a load cell, ρ_a the air density (around 1.18kg/m^3 at 25°), U_{ref} the velocity of the approaching wind measured using the Pitot tube, and A_c the projected frontal area of the tree. Increasing U_{ref}, the drag coefficient converges to a constant value equal to 0.65, which is in line with the

drag coefficient of a real tree (Manickathan et al., 2018), for Reynolds numbers based on the tree ($Re_t = U_{ref} H_T/\nu$, where H_T is the tree height) greater than 10^4. The model trees were inserted in the reference canyon, arranged according to three different configurations: no trees inside the canyon (Zero, Fig. 1b), two parallel rows of seven trees spaced 14 cm apart (Half, Fig. 1c) and two parallel rows of fourteen trees spaced by 7 cm (Full, Fig. 1d).

3 Measurement techniques

We used the Laser Doppler Anemometer (LDA) technique, to measure the streamwise (u), transversal (v), and vertical (w) components of the velocity field. As detailed below, we first measured simultaneously u and v inside the canyon only, then we coupled a mirror to the LDA to measure u and w both inside the canyon and at the roof level. In a third measuring session, the system LDA-mirror was coupled with a Flame Ionization Detector (FID) to measure vertical turbulent mass fluxes, both inside the canyon and at the rooftop. The concentration field was measured with high spatial resolution by means of the FID alone (Fellini et al., 2022).

3.1 Concentration

The scalar concentration was measured using a FID model HFR400, suitable to measure hydrocarbon concentration time series. The instrument is equipped with a sampling capillary tube 0.3 m long, 1.27×10^{-4} m inner radius, and imposed pressure drop of 33330.6 Pa, guaranteeing a frequency response of about 800 Hz (Nironi et al., 2015). The FID works in the range 0-10 V, and it detects concentration values in the range 0-5000 ppm, with a precision of about 1-2 ppm. The relation between the electric potential measured by the FID and the concentration in ppm is a linear function, whose slope coefficient is calculated by calibrating the instrument at the beginning and at the end of each measurement session (Marro et al., 2020). A variation of $\pm 3\%$ of the coefficient is accepted, as the instrument is sensitive to ambient conditions. Since the wind tunnel is a recirculating system, the background concentration increases with time. Thus, a linearly interpolated value of the background concentration recorded at the beginning and at the end of each measurement is subtracted from the concentration signals.

The scalar field was characterized using a three-dimensional measuring grid, whose details are available in Fellini et al. (2022). In the present work, we extract from that dataset a 2D vertical section in the center of the canyon (x/H=1), and a 2D horizontal section at the rooftop (z/H=1). The measurements were performed setting a constant sampling frequency of 1000 Hz and an acquisition time of 120 s. Analysing concentration signals, we verified that the acquisition time is enough

long to guarantee a good convergence of the mean and standard deviation of the concentration. To collect more samples for the investigation of the probability density function of the concentration, we extended the acquisition time to 300 s for a limited number of sampling points located along a longitudinal profile in the center of the canyon (x and z coordinates were fixed at x/H=1 and z/H=0.4, respectively). In the vegetated canyon configurations, a higher number of sampling points were measured, to capture the heterogeneity of the mean concentration profiles.

3.2 Velocity

The velocity field was measured using a LDA Argon class IV, equipped with a 5 W power laser, emitting two blue and two green beams with wavelengths λ_{blue}=488 nm and λ_{green}=514.5 nm, respectively. The beams have a diameter of 0.1 mm and the LDA focal length is 400 mm. The point of intersection of the four beams determines the measuring volume. In dual-beam configuration, the LDA provides the module and the direction of two velocity components simultaneously, notably u and v. To measure the u component together with w, the LDA is coupled with a mirror, which deflects the laser beams (as shown in Fig. 1e). We maintained a data rate of around 1500 Hz, and a sampling time sufficiently long to collect at least 250 000 samples in each measuring point, to obtain a good convergence of the statistical moments of the velocity signal. During the acquisition, the power of the blue and the green beams was set at 800 mW. The seeding of the flow was generated with the fluid SAFEX®-Inside-Nebelfluid "Dräger Spezial W", emitting droplets with dimensions in the range 0.5-2 μm.

3.3 Turbulent mass flux

The turbulent vertical mass fluxes are evaluated as the cross-correlation between concentration fluctuations and velocity fluctuations, $c'(t)$ and $w'(t)$, respectively. Instantaneous fluctuations are defined as $c'(t) = c(t) - \overline{c}$ and $w'(t) = w(t) - \overline{w}$ respectively, where $c(t)$ is the concentration time series with the background concentration removed (see section 3.1), $w(t)$ is the vertical velocity time series, $\overline{c}$ and $\overline{w}$ are their mean, and t is the time. The estimate of cross-correlation requires concentration and velocity to be measured simultaneously, in the same control volume. This can be achieved by coupling the FID and the LDA (Fig. 1e).

The installation of the LDA-FID system and the evaluation of the cross-correlation were performed following the approaches and methods provided by Marro et al. (2020). The distance between the measuring volume of the LDA and the sampling tube of the FID was set at 4 mm, as it is the optimal distance to avoid flow disturbances caused by the FID and to guarantee that concentration and velocity measurements refer to the same fluid elements. In this setup, the time delay between

the two signals (Δt_{lag}), due to the travel of the particles across the sampling tube (see subsection 3.1), was estimated to be 0.016 s (Marro et al., 2020). The cross-correlation between velocity and concentration fluctuations ($\overline{w'c'}$) was computed using the sample-and-hold reconstruction and resampling (S+H) method (Kukačka et al., 2012; Marucci and Carpentieri, 2019). Notably, the concentration signal was shifted by Δt_{lag}, and resampled on the irregular sampling frequency of $w(t)$, using the nearest neighbor interpolation since the correspondence between velocity and concentration data was missing. This method is reliable in this application, as it provides results with less than 6% difference from those of the well-established slot correlation method (Marro et al., 2020).

Flow velocity and turbulent mass fluxes were measured on a 2D vertical grid along the longitudinal axis of the canyon (the streamwise coordinate is fixed at x/H=1) and on a horizontal grid at the rooftop (fixing the vertical coordinate at z/H=0.98). The vertical grid, being located in the centre of the canyon, is easily accessible to the experimental equipment (in particular the system LDA-FID coupled with the mirror) in both the empty and vegetated canyons, the horizontal grid, fixed 2 mm below the canyon rooftop, is used to investigate the flow field and mass transfer between the inner canyon and the external atmosphere. The vertical grid at x/H=1 is composed of five longitudinal profiles sampled at heights z/H=[0.2, 0.4, 0.6, 0.8, 0.98], whilst the horizontal section at the rooftop includes three longitudinal profiles at x/H=[0.5, 1, 1.5]. Both sections extend from y/H=–3.5 to y/H=+3.5. The longitudinal spacing of the sampling points is 50 mm in the Zero configuration, while it is irregular in the vegetated canyon configurations, due to the encumbrance of trees, and due to the fact that the mean scalar field is not homogeneous, so more points were acquired in correspondence of the mean concentration peaks (Fellini et al., 2022).

4 Results

In this section, we investigate the influence of tree density on the flow velocity (Fig. 4-6), concentration statistics (Fig. 7-11), and mass fluxes (Fig. 12-15). The mean and the turbulent components of all quantities are shown on vertical and horizontal sections (located at x/H=1 and z/H=0.98 or z/H=1, respectively), both obtained from linear interpolation of measured data. Moreover, using instantaneous concentration, velocity, and mass fluxes data we evaluate the concentration probability density function inside the canyon (Fig. 11) and the spectra of vertical velocity fluctuations and turbulent mass fluxes at the rooftop (Fig. 6, 15).

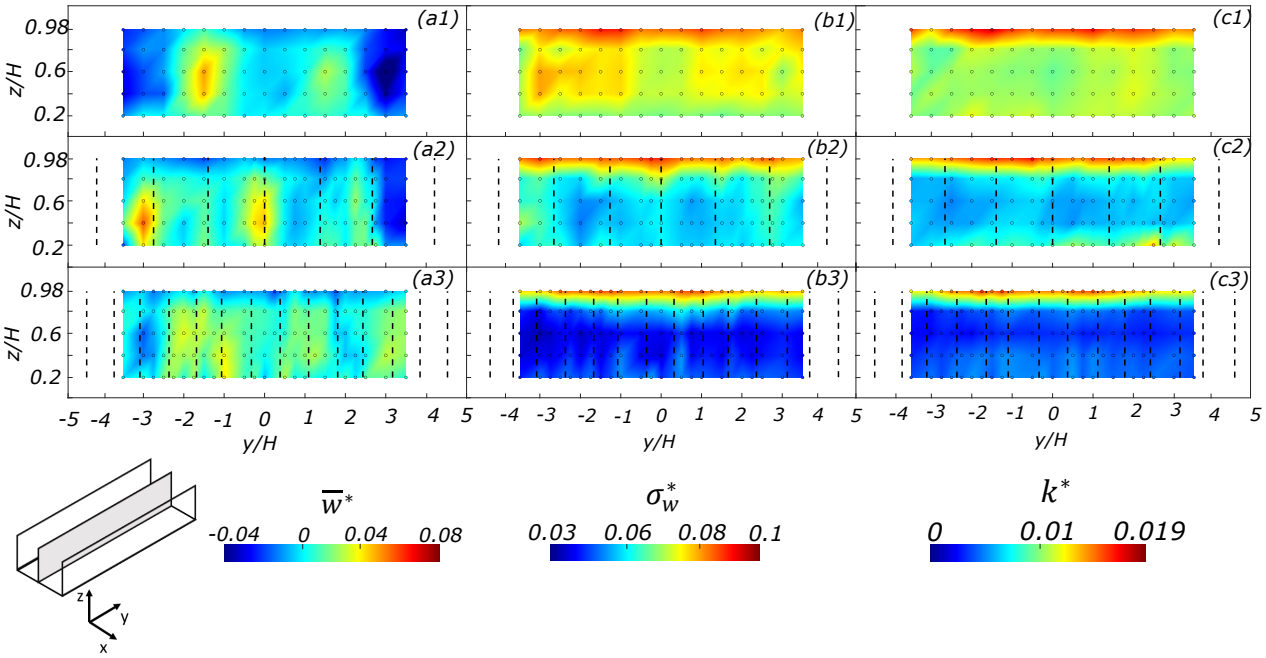

Figure 4: Two-dimensional sections of mean vertical velocity (a1-a3), vertical velocity standard deviation, (b1-b3) and turbulent kinetic energy (c1-c3), on the plane at x/H=1. The Zero (a1, b1, c1), Half (a2, b2, c2), and Full (a3, b3, c3) configurations are shown. Black dashed lines indicate the position of the trees. Colored circles represent the measuring points. The shaded area in the sketch shows the position of the cross-section in the canyon.

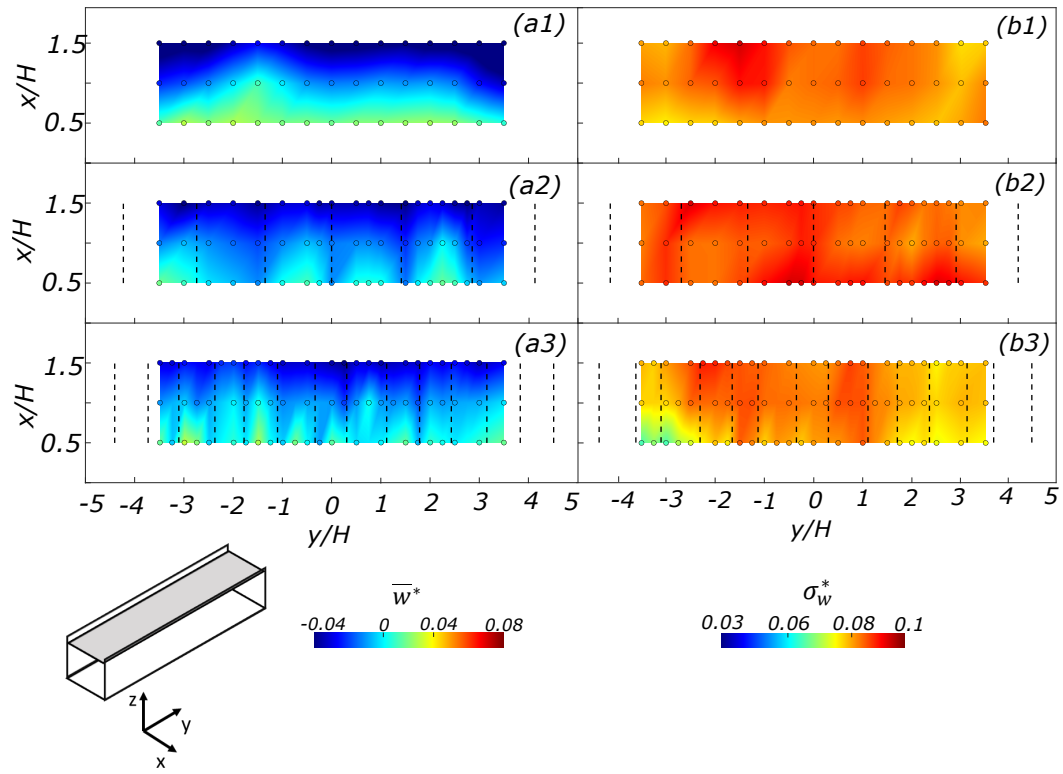

Figure 5: Two-dimensional sections of mean vertical velocity (a1-a3) and vertical velocity standard deviation (b1-b3), on the plane at z/H=0.98. The Zero (a1, b1), Half (a2, b2), and Full (a3, b3) configurations are shown. Black dashed lines indicate the position of the trees. Colored circles represent the measuring points. The shaded area in the sketch shows the position of the cross-section in the canyon.

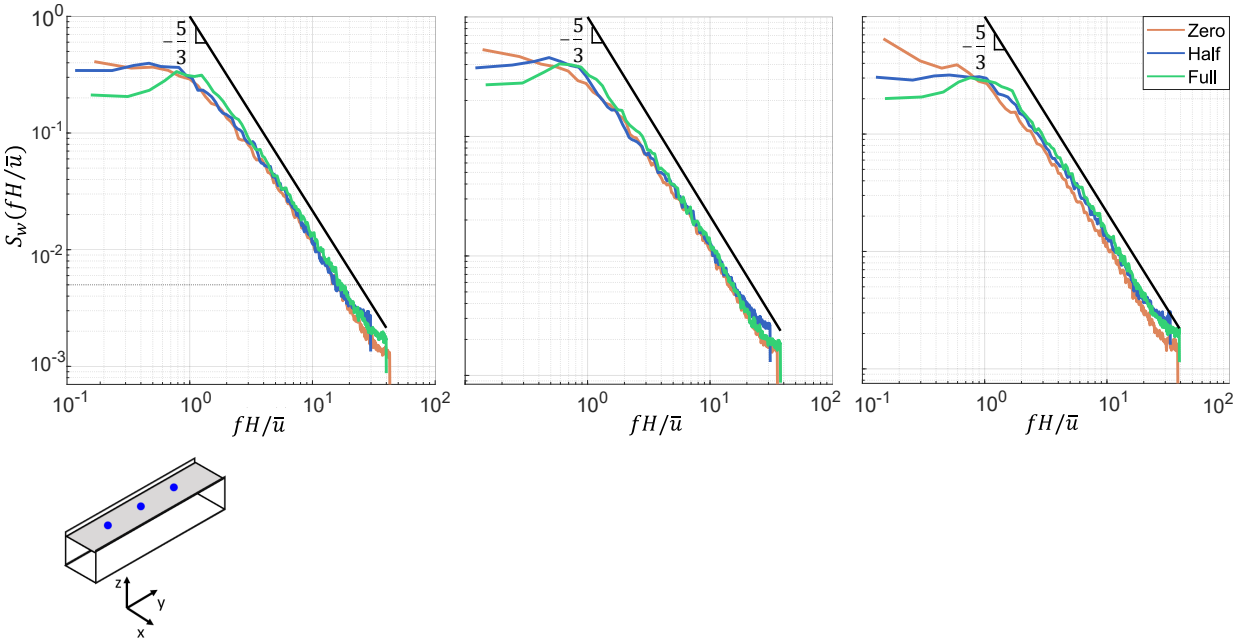

Figure 6: Spectra of $w'(t)$ calculated in three different sampling points along the central line (x/H=1) at the rooftop (z/H=0.98): (a) y/H=-1.5, (b) y/H=0, (c) y/H=2. The blue points on the shaded plane in the bottom inset represent the positions where the spectra were calculated.

4.1 Flow field

As we are interested in analyzing the vertical mass transport in the street canyon, we focus here on the spatial distribution of the mean and standard deviation of the vertical velocity, normalized as $(\overline{w}^*, \sigma_w^*) = (\overline{w}, \sigma_w)/U_\infty$, respectively. Positive $\overline{w}^*$ refers to upward flow and negative $\overline{w}^*$ refers to downward flow. As we mentioned in section 3, we measured also u and v components.

Figure 4a1-a3 show the mean vertical velocity in the center of the canyon. In the Zero configuration (panel a1), the $\overline{w}^*$ field is organized in two symmetric zones of upward flow (around y/H=–1.5 and y/H=+1.5), and three zones of downward flow located at the edges and in the center of the canyon. The asymmetries in the upward flow regions, are due to tiny uncertainties in the arrangement of the building-like blocks (Garbero et al., 2010) and slight inclination of the external flow with respect to the wind tunnel axis (Nironi et al., 2015). In the Half configuration (panel a2) the succession of positive and negative zones is still present, but the spatial organization is different: we identify three zones of positive $\overline{w}^*$ and two zones of negative $\overline{w}^*$. In the Full configuration (panel a3), positive $\overline{w}^*$ values prevail and the spatial pattern is more homogeneous. The mean flow within a urban canyon perpendicular to the external wind flow is governed by a recirculating cell (Gromke and Ruck, 2007; Fellini et al., 2022) as the external flow enters the canyon at the downwind wall and exit at the upwind wall. As a consequence, moving toward the downwind wall of the street canyon, we expect a downward flow to occur and the presence of trees to lead to a more heterogeneous pattern. Moreover, due to the recirculation we do not observe a decrease in the mean vertical velocity moving towards the ground level. The random shape, size, and orientation of the model trees produce further asymmetries, even if they are smaller than the different longitudinal patterns induced by the different tree spacing.

Conversely, vegetation does not induce peculiar spatial patterns in the vertical velocity standard deviation (Fig. 4b1-b3): σ_w^* remains fairly constant, both along the y and z axes, until the interface between the canyon and the external flow ($z/H = 0.98$) where it increases sharply, and it reaches the same value (about 0.08) in all configurations. On average, below the tree crowns, σ_w^* decreases with the increase in tree density: in the Full configuration, the spatial average of σ_w^* (calculated by weighting the single values by the area associated to each measurement point) is 40% lower than in the Zero configuration.

In panels c1-c3 of Fig. 4, we analyze the turbulent kinetic energy, estimated as $k^* = 0.5(\sigma_u^2 + \sigma_v^2 + \sigma_w^2)/U_\infty^2$. In the Zero and Full configurations (panels c1 and c3), k^* is homogeneous in the interval z/H=[0.2, 0.8]. In the Half configuration (panel c2) it is slightly heterogeneous moving along the vertical direction: higher close to the ground and lower in the interval z/H=[0.4, 0.8]. The enhanced values of k^* observed close to the ground are due to the fact that the dampening effect is

mainly limited in correspondence of the tree crowns, while the large spacing between trunks allows the k^* to slightly recover the intensity it has in the empty canyon. As observed for σ_w^* (panels b1-b3), the presence of trees dampens k^*: on average, we observe a decrease of 60% between Zero and Full configurations. Moving to the rooftop of the canyon (z/H in the interval [0.8, 0.98]), we identify a sharp increase of k^*, regardless of the presence of trees. The increase of both k^* and σ_w^* reveals the presence of a shear layer of thickness $z/H \sim 0.2$, where the turbulence of the external flow is entrained in the cavity flow (Salizzoni et al., 2011; Fellini et al., 2020).

An evident imprinting of the trees can be noticed by comparing the mean vertical velocity patterns at the rooftop among the different configurations (Fig. 5a1-a3). In the non-vegetated canyon (panel a1), $\overline{w}^*$ has a quite homogeneous behavior along the y-axis: negative at the downwind wall, and positive at the upwind wall. Indeed the external flow enters the canyon at the downwind wall and leaves it at the upwind wall, following a recirculating flow structure (Gromke and Ruck, 2009). In the vegetated canyons, this pattern is maintained, but it is more heterogeneous at the upwind wall, as trees hinder the vertical flow motion: the upward flow occurs between adjacent trees, and its spatial periodicity increases with tree density (panels a2, a3).

On the other hand, the values of σ_w^* at the rooftop (Fig. 5b1-b3) are almost unaffected by the presence of trees. In the Zero and Half configurations (panels b1 and b2), σ_w^* values are almost homogeneous both in the longitudinal and streamwise directions. In the Full configuration (panel b3), some heterogeneities arise: σ_w^* decreases moving towards the edges of the canyon, mostly at the left upwind corner. In all configurations, σ_w^* values are significantly higher than the one inside the canyon.

To investigate the influence of trees on the scales of the turbulent structures involved in the energy motion at the rooftop of the canyon, we analyze the spectra of the vertical velocity signal, calculated with the Welch method. Once resampled the $w(t)$ signal at a constant sampling frequency of 1000 Hz, the Fourier transform was applied to windows of 500 samples (filtered with the Hamming filter), in order to obtain well-resolved spectra without losing information in the low-frequency range. The final spectrum is the mean of the spectra calculated in each window. In Fig. 6, we report the velocity spectra, calculated in three sampling points along the central profile at the rooftop of the canyon: two points in correspondence of the concentration peaks (y/H=–1.5 and y/H=2, as will be shown in section 4.2) and one point in the centre (y/H=0). The three different curves represent the velocity spectra (S_w) in the Zero, Half, and Full configurations, expressed as a function of the non-dimensional frequency $fH/\overline{u}$. To compare spectra in different vegetation configurations, we referred to the velocity signal normalized as $(w(t)-\overline{w})/\sigma_w$, so that the three curves have the same subtended area, equal to 1. Spectra show a decrease

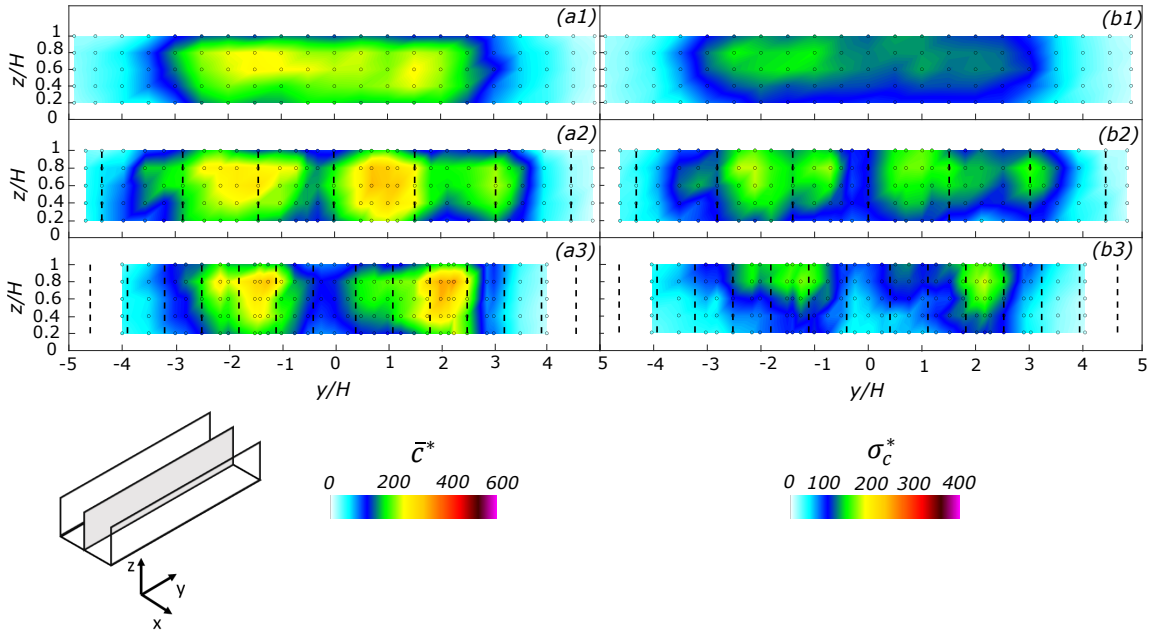

Figure 7: Two-dimensional sections of mean concentration (a1-a3) and concentration standard deviation (b1-b3), on the plane at x/H=1. The Zero (a1, b1), Half (a2, b2), and Full (a3, b3) configurations are shown. Black dashed lines indicate the position of the trees. Colored circles represent the measuring points. The shaded area in the sketch shows the position of the cross-section in the canyon.

in the energy content of the large-scale structures (non-dimensional frequencies in the range 10^{-1}-10^{0}) when the canyon is vegetated, that are likely be responsible for the reduced σ_w^* levels induced by high tree density at the canyon rooftop (pointed out in Fig. 5b3). The decrease in energy associated with large scales with tree density can be attributed to the fact that the characteristic length scales of turbulence are significantly influenced by the decreasing tree spacing observed in the Zero, Half, and Full configurations. Conversely, if we look at length scales of the order of magnitude smaller than the tree spacing (namely, non-dimensional frequencies larger than around 0.7 and 1.4 for the Half and Full configurations, respectively), the three curves overlap meaning that the effect of the vegetation density is no more detectable. Indeed, at intermediate scales ($fH/\overline{u} = 10^{0}$-10^{1}) the three spectra show an evident inertial region with constant slope proportional to -5/3 (the characteristic Kolmogorov inertial scaling), regardless of the tree density.

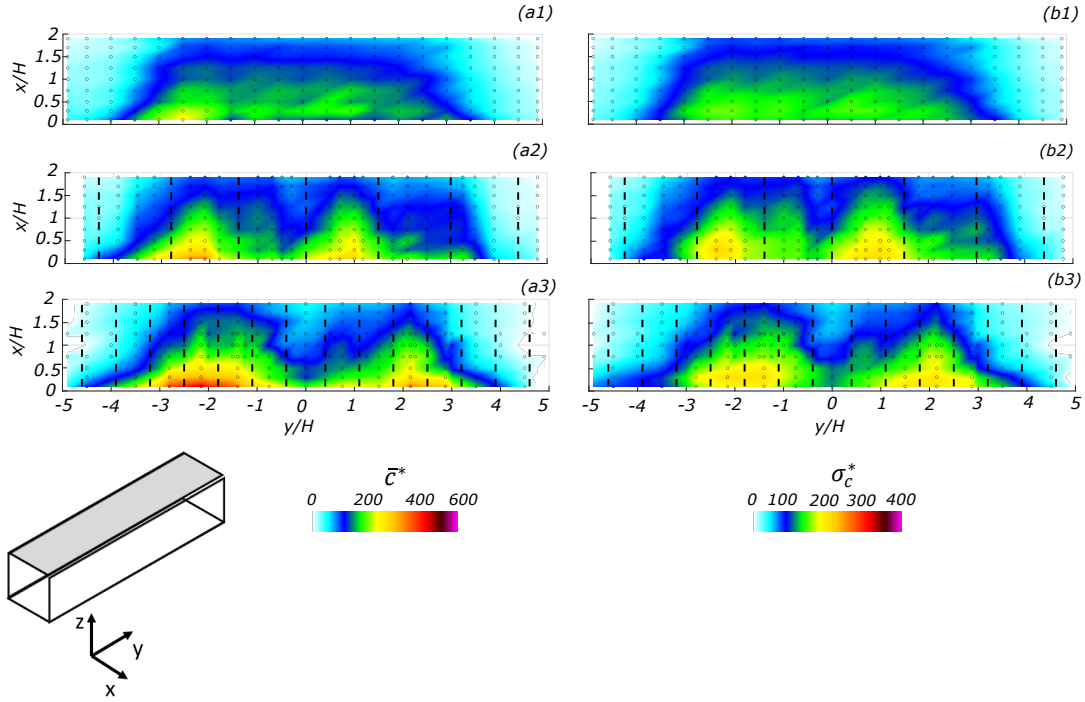

Figure 8: Two-dimensional sections of mean concentration (a1-a3) and concentration standard deviation (b1-b3), on the plane at z/H=1. The Zero (a1, b1), Half (a2, b2), and Full (a3, b3) configurations are shown. Black dashed lines indicate the position of the trees. Colored circles represent the measuring points. The shaded area in the sketch shows the position of the cross-section in the canyon.

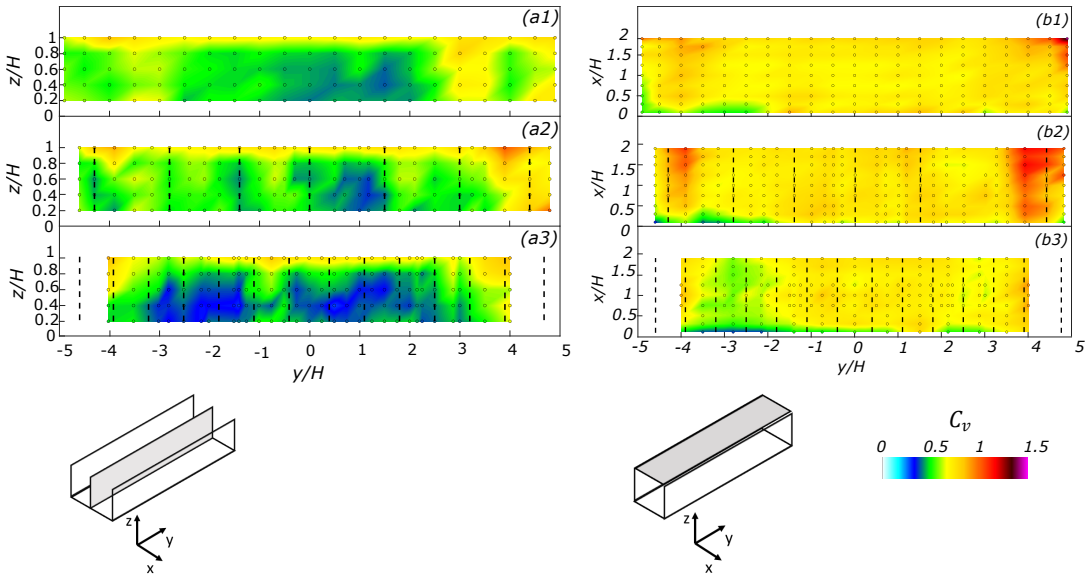

Figure 9: Two-dimensional sections of the coefficient of variation of the concentration on the plane at x/H=1 (left column) and z/H=0.98 (right column). The Zero (a1 and b1), Half (a2 and b2), and Full (a3 and b3) configurations are shown. Black dashed lines indicate the position of the trees. Colored circles represent the measuring points. The shaded area in the sketch shows the position of the cross-section in the canyon.

4.2 Concentration field

As a first step, we recall the main features of the mean concentration field (investigated in detail by Fellini et al., 2022) and, then, we analyze the concentration standard deviation and the coefficient of variation (Fig. 7-9). We use the non-dimensional form $(\overline{c}^*, \sigma_c^*) = (\overline{c}, \sigma_c) U_\infty \delta L_s / Q_{et}$, where $\overline{c}$ and σ_c are the mean and the standard deviation of the concentration time series, respectively, δ is the height of the boundary layer, L_s is the source length and Q_{et} is the ethane mass flowrate.

Inside the canyon, we notice that, in the range $y/H = [-3, 3]$, the presence of trees induces a transition from a rather homogeneous mean concentration field to a heterogeneous one (panels a1-a3 of Fig. 7), along the longitudinal axis. The Half configuration (panel a2) exhibits three zones of higher mean concentration, whilst the Full configuration (panel a3) is characterized by two nearly symmetric accumulation zones and a well-defined area of low concentration in the centre of the canyon: here, the concentration is approximately half the one measured in the accumulation zones. The increase in the spatial heterogeneity of pollutant concentration with tree density is in contrast with the behavior of the mean velocity field (shown in Fig. 4a1-a3), which tends to homogenize with the increase in tree density. Notice that, at the edges, $\overline{c}^*$ has very low values because the line source does not cover the entire length of the street canyon. Conversely, the mean concentration does not decrease going farther away from the ground-level source, as the pollutant is transported within the canyon by a recirculating structure. For a detailed analysis of the mean scalar field, see Fellini et al. (2022). The increased variability in the mean concentration field arises from the complex interaction between larger-scale motions and the smaller eddies within the canyon, which are generated by the presence of trees. Given this context, there are reservations about the suitability of relying on a single parameter, such as the bulk vertical exchange velocity (u_d), which requires averaging concentrations within the canyon, to assess the canyon's ventilation potential.

The standard deviation of the concentration (Fig. 7b1-b3) follows almost the same patterns observed for the mean concentration field: a quite homogeneous trend in the spatial range $y/H = [-3, 3]$ for the Zero configuration (panel b1) and concentration fluctuation peaks when trees are added (panels b2 and b3). However, some differences can be pointed out: σ_c^* decreases slightly along the y-axis in the non-vegetated canyon and shows an increasing trend in the vertical direction, mostly in the correspondence of peaks in the Full configuration. Differently from σ_w^* (Fig. 4b1-b3), the average σ_c^* does not follow a well-defined decreasing trend with vegetation density: with respect to the Zero configuration, the spatial average of σ_c^* increases of 18% in the Half configuration and decreases of 6% in the Full configuration. However, the local maxima of σ_c^* are larger in the presence of trees (see green areas in Fig. 7b2,b3).

The mean concentration and the concentration standard deviation patterns are similar also at the rooftop (Fig. 8). Both show a clear positive gradient from the downwind wall to the upwind wall, which is almost constant along the y-axis in the non-vegetated canyon (panels a1 and b1), while it presents accumulation zones at the upwind wall in the Half and Full configurations (panels a2, b2, a3 and b3). These high concentration areas enhance the difference in $\overline{c}^*$ and σ_c^* between the two walls: in the Zero configuration, the spatial average of $\overline{c}^*$ at the upwind wall is 58% higher than the one at the downwind wall (note that this is computed by weighting the single value by the spacing between the measurement points along the profiles at x/H=0.1 and x/H=1.9, respectively), and this difference reaches 66% and 75% in the Half and Full configurations, respectively. For the concentration standard deviation, the difference between the walls is 52%, 57%, and 65% in the Zero, Half, and Full canyons, respectively. As we observed inside the canyon, the presence of vegetation increases the local maxima of σ_c^* (see yellow areas in panels b2 and b3).

In order to highlight differences between mean and standard deviation patterns, in Fig. 9, we investigate the spatial distribution of the coefficient of variation of the concentration, defined as $C_v = \sigma_c/\overline{c}$. As we will see in section 4.2.1, C_v is a key parameter in the analytical models for the probability density function of the scalar concentration in dispersing plumes (Orsi et al., 2021). Inside the canyon (panels a1-a3), the coefficient of variation shows very similar spatial distributions in the Zero and Half configurations, with lower values close to the centre (blue region) and increasing values moving toward the lateral edges of the canyon. Here, the mean and the fluctuating component of the concentration are very low, as there is no scalar emission from the source, thus the evaluation of C_v is affected by large uncertainty. In the Full configuration (panel a3), we observe two regions characterized by weak C_v values, leading to an average decrease of 11% with respect to the Zero configuration. The vegetation-induced transition from a homogeneous field to a heterogeneous one is not as pronounced as for $\overline{c}^*$ and σ_c^* fields, where we observed local differences up to 50% in the Full configuration (see Fig. 7a3,b3), however, the high tree density slightly dampens the concentration fluctuations around the mean, leading to a more heterogeneous pattern with respect to Zero and Half configurations.

At the rooftop (panels b1-b3), C_v is almost homogeneous in all configurations, and 40% larger than within the canyon. However, some heterogeneities appear: higher C_v values at the edges of the canyon and an area of lower C_v around $y/H = -3$ in the Full configurations. Again, the heterogeneities are linked to the uncertainty in the C_v estimate due to the low concentration measured laterally.

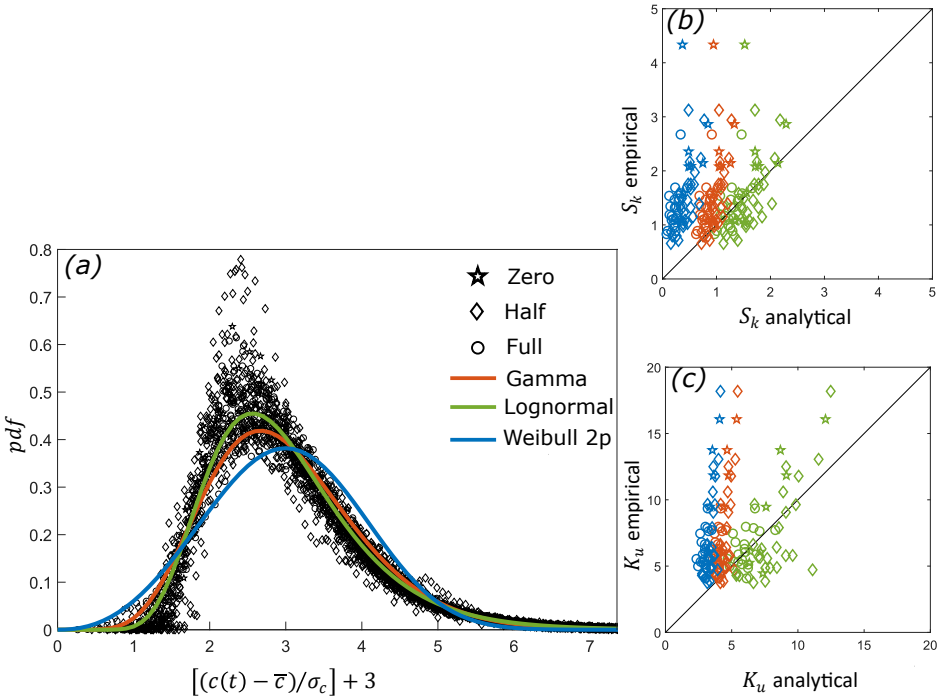

Figure 10: (a) Empirical pdfs fitted by the gamma (orange), lognormal (green), and Weibull 2p (blue) distributions. The Zero, Half, and Full configurations are considered. (b,c) Scatterplots that compare analytical and empirical skewness and kurtosis.

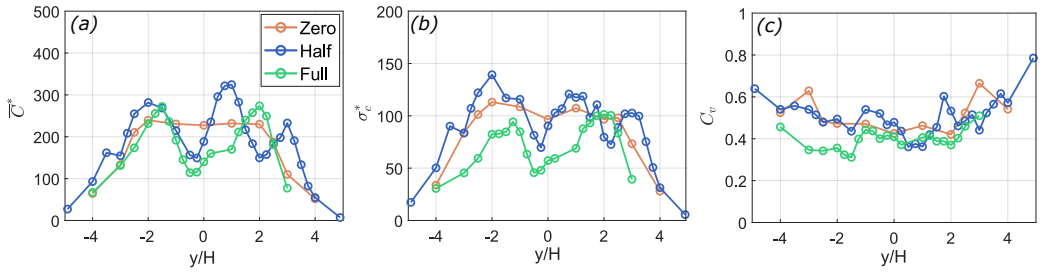

Figure 11: Longitudinal profile at x/H=1 and z/H=0.4 of (a) mean concentration, (b) concentration standard deviation, (c) coefficient of variation of the concentration, calculated from the long concentration time series. The Zero (orange), Half (blue), and Full (green) configurations are shown.

4.2.1 Concentration probability density function

The characterization of the probability density function (pdf) of pollutant concentration has several applications including the evaluation of the health risks related to the exposure to high levels of toxic substances, odors assessment, or the estimation of the upcrossing probability. Indeed, these questions require the knowledge of the occurrence probability of instantaneous concentration values above critical thresholds, and, therefore, information about the pdf. Previous studies investigated the pdf of concentration fluctuations arising from localised releases in the atmospheric boundary layer (see the review of Cassiani et al., 2020). Nironi et al. (2015) carried out measurements of concentration fluctuations inside a plume released by a point source, considering different source sizes and elevations. They found that the empirical pdf changes shape with distance from the source, and is well modeled by a gamma distribution. Other studies report that the lognormal distribution is a suitable model for plume dispersion in neutral boundary layers (Yassin, 2008; Finn et al., 2010), while the two- and three-parameter Weibull distributions provide analytical formulations to estimate the percentiles of the concentration, who have important applications in the odor assessment (Oettl and Ferrero, 2017). Conversely, releases by linear sources were poorly investigated. Li and Bilger (1996) calculated the statistical moments of the scalar concentration behind a line source and they found that the empirical pdf is skewed to the right near the source and it is symmetrical and close to a Gaussian in the far field. Sawford and Stapountzis (1986) compared the pdf calculated from wind-tunnel measurements of concentration of heat, downstream of a line heating source (performed by Stapountzis et al., 1986), with a one-dimensional fluctuating model.

To fill this gap, we performed a statistical analysis of the pdf of long concentration time series, measured along longitudinal profiles in the centre of the canyon (see Section 3.1). To compare the pdfs calculated in different spatial points and different configurations, we adopt the sample space variable $\chi(t) = c(t)/\overline{c}$. By means of the method of moments, we fitted the empirical pdfs with the three analytical distributions mentioned above, that proved suitable to model the passive scalar concentration pdf in turbulent flows (as mentioned above): the gamma distribution, the lognormal distribution and the two-parameters Weibull distribution (Weibull 2p). The analytical pdfs can be commonly expressed as a function of the unique parameter, C_v:

1. gamma distribution:

$$P(\chi, \vartheta) = \frac{\vartheta^{\vartheta}}{\Gamma(\vartheta)} \chi^{\vartheta - 1} \exp(-\vartheta\chi) \tag{4}$$

   where $\Gamma(\cdot)$ is the gamma function and ϑ is the the shape parameter, defined as $\vartheta = C_v^{-2}$.

2. lognormal distribution:

$$P(\chi, C_v) = \frac{1}{\chi\sqrt{2\pi \ln(1+C_v^2)}} \exp\left\{-\frac{\left[\ln(\chi) + \ln\left(\frac{1}{\sqrt{1+C_v^2}}\right)\right]^2}{2\ln(1+C_v^2)}\right\} \tag{5}$$

3. Weibull 2p distribution:

$$P(\chi, C_v) = \frac{C_v^{-1.086}}{a_w}\left(\frac{\chi}{a_w}\right)^{C_v^{-1.086}-1} \exp\left[-\left(\frac{\chi}{a_w}\right)^{C_v^{-1.086}}\right] \tag{6}$$

where a_w is the scale parameter, which can be approximated as a function of C_v (Orsi et al., 2021):

$$a_w = \frac{1}{\Gamma(1+C_v^{1.086})} \tag{7}$$

The goodness-of-fit between the empirical and analytical distributions was evaluated calculating the mean absolute error between the empirical cumulative distribution function (cdf) and the gamma, lognormal, and Weibull 2p cdfs. Comparing the mean absolute errors (reported in tables 1-3 in the supplementary material), we found that, in all spatial points and in all the tree density configurations, the largest absolute error is associated to the Weibull 2p distribution. This result was expected in the presence of a linear source, as the Weibull 2p distribution approximates the concentration pdf close to a point source where the meandering dominates the dispersion process (Orsi et al., 2021). Conversely, the lowest mean absolute error is associated to the lognormal distribution in the 80% of the spatial points in the Zero configuration, in the 70% in the Half configuration, and in the 100% in the Full configuration. In the Zero and Half configurations, also the gamma distribution is a suitable model, indeed it shows a mean absolute error comparable to the one associated to the lognormal distribution in the 60% of the spatial points in the Zero configuration and in the 40% in the Half configuration.

The empirical pdfs together with the lognormal, gamma, and Weibull 2p distributions are reported in Fig. 10a. Here, the concentration time series were normalized as $[(c(t) - \overline{c})/\sigma_c] + 3$, to collapse all the distributions calculated along the longitudinal profiles into a single distribution with zero mean and unit variance. As the analytical distributions do not fit negative concentration fluctuations, the normalized concentration was shifted by a constant equal to 3. The empirical pdfs show a positive skewed bell-shaped behavior in all spatial points. The same shape is observed in the Zero, Half and Full configurations, hence it is not affected significantly by vegetation density. A qualitative observation of the overlap between analytical models and empirical pdfs confirms that the Weibull 2p distribution is

the worst model, while both the gamma and lognormal distributions reproduce well the empirical pdfs, despite some discrepancies in the peak and in the left tail. The similarity among the pdfs is due to the fact that the longitudinal profiles of C_v (which is the only parameter that appears in equations 4-6) show variations of the order of 6% (Fig. 11c), so they can be considered homogeneous along y-axis, as the variations are small compared to the local variations (up to 50%) found in the mean and turbulent concentration profiles (Fig. 11a,b).

We investigated the quality of the fitting also considering the third and fourth moments. The equations of the analytical skewness (S_k) and kurtosis (K_u) as a function of C_v are provided in Appendix 1. In panels b and c of Fig. 10, we report the scatter plots of the analytical versus empirical skewness and kurtosis, respectively. The skewness is higher than zero, revealing that the pdfs are skewed to the right. The kurtosis is higher than 3, so the distributions have fatter tails than the Gaussian distribution. The empirical skewness and kurtosis are underestimated by the analytical functions provided by both the Weibull 2p and the gamma distributions. On the other hand, a non-biased estimation of the empirical moments is obtained from the lognormal distribution. Indeed, the scatter plot shows a good correlation between the empirical skewness and kurtosis with the analytical ones, mostly in the Full configuration. We can, therefore, conclude that the lognormal distribution performs a better fitting of the empirical skewness and kurtosis, and of the entire pdf, especially with high tree density.

4.3 Vertical mass transport

We decompose the vertical mass flux ($\overline{wc}$) in the mean component ($\bar{w}\bar{c}$) and the turbulent component ($\overline{w'c'}$) (Fischer et al., 1979). The latter corresponds to the cross-correlation between velocity and concentration fluctuations measured in the same control volume (see Section 3.3).

Figure 12 shows the non-dimensional mean, turbulent and total mass fluxes (where vertical velocity and concentration are normalised as defined in the previous sections), evaluated in the inner canyon. The behavior of the mean vertical fluxes (Fig. 12a1-a3) is similar to that of the mean vertical velocity (observed in Fig. 4a1-a3), characterized by a well-organized spatial pattern in the non-vegetated canyon, that is partially lost increasing the tree density. In the Zero configuration (panel a1 of Fig. 12), the mean mass flux is positive in two symmetric regions in the centre of the canyon and negative close to the edges. The Half configuration (panels a2) is characterized by three zones of positive mean flux, and three less extended zones of slightly negative flux. In the Full configuration (panels a3), the mean flux is positive almost in the whole section, except for an area close to the left edge where it is negative. Turbulent mass fluxes transport mass down homogeneously in the Zero configuration (panel b1) and in between the trees in the Half configuration

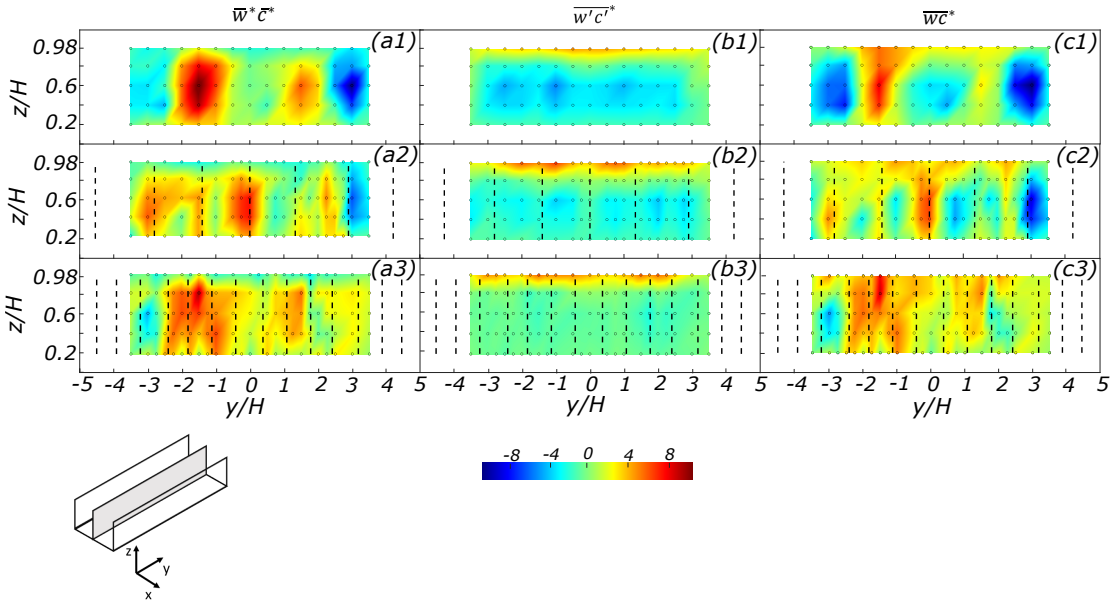

Figure 12: Two-dimensional sections of convective (a1-a3), turbulent (b1-b3), and total (c1-c3) mass fluxes on the plane at x/H=1. The Zero (a1, b1, c1), Half (a2, b2, c2), and Full (a3, b3, c3) configurations are shown. Black dashed lines indicate the position of the trees. Colored circles mark the measuring points. The shaded area in the sketch shows the position of the cross-section in the canyon.

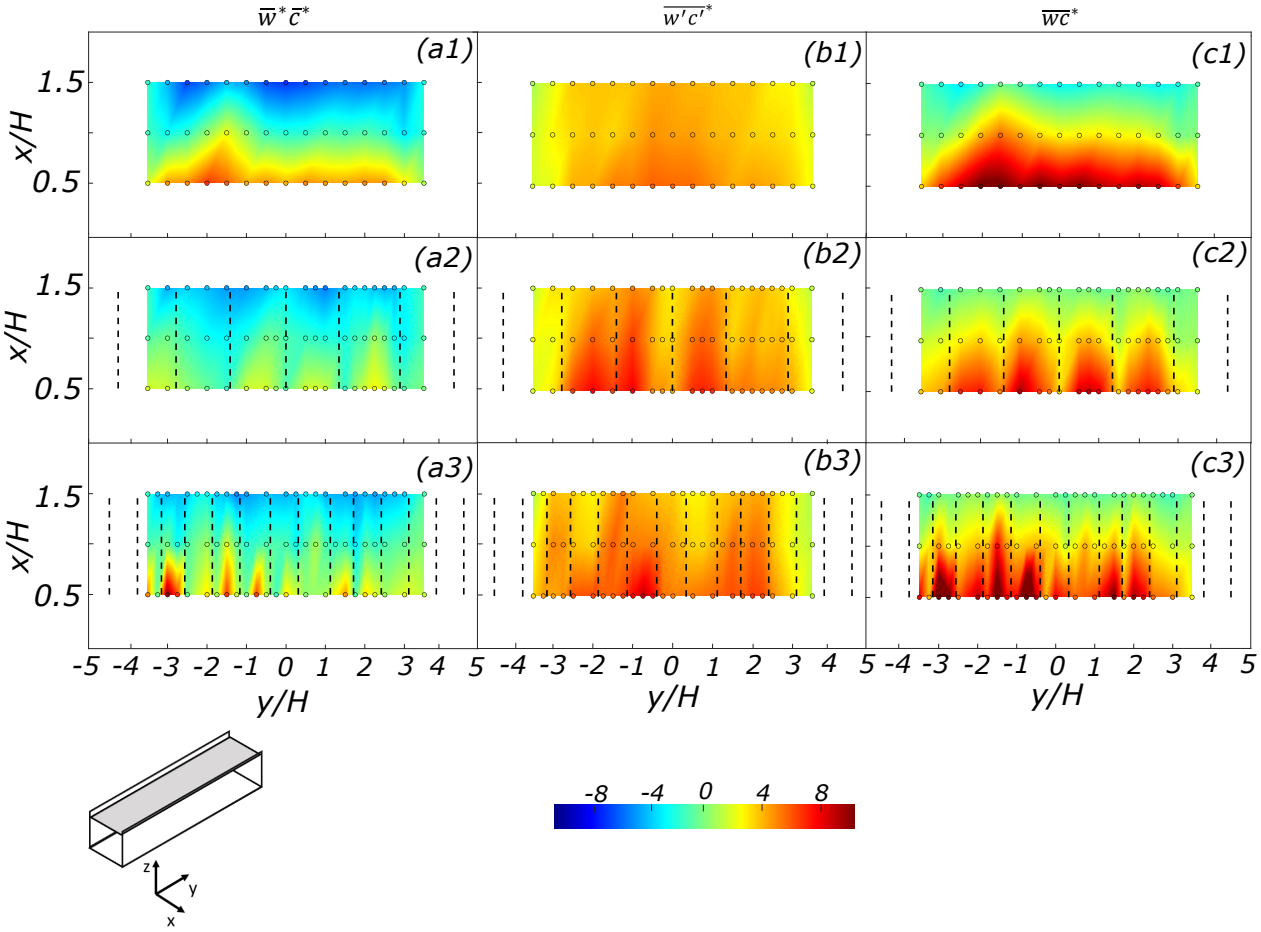

Figure 13: Two-dimensional sections of convective (a1-a3), turbulent (b1-b3), and total (c1-c3) mass fluxes on the plane at z/H=0.98. The Zero (a1, b1, c1), Half (a2, b2, c2), and Full (a3, b3, c3) configurations are shown. Black dashed lines indicate the position of the trees. Colored circles mark the measuring points. The shaded area in the sketch shows the position of the cross-section in the canyon.

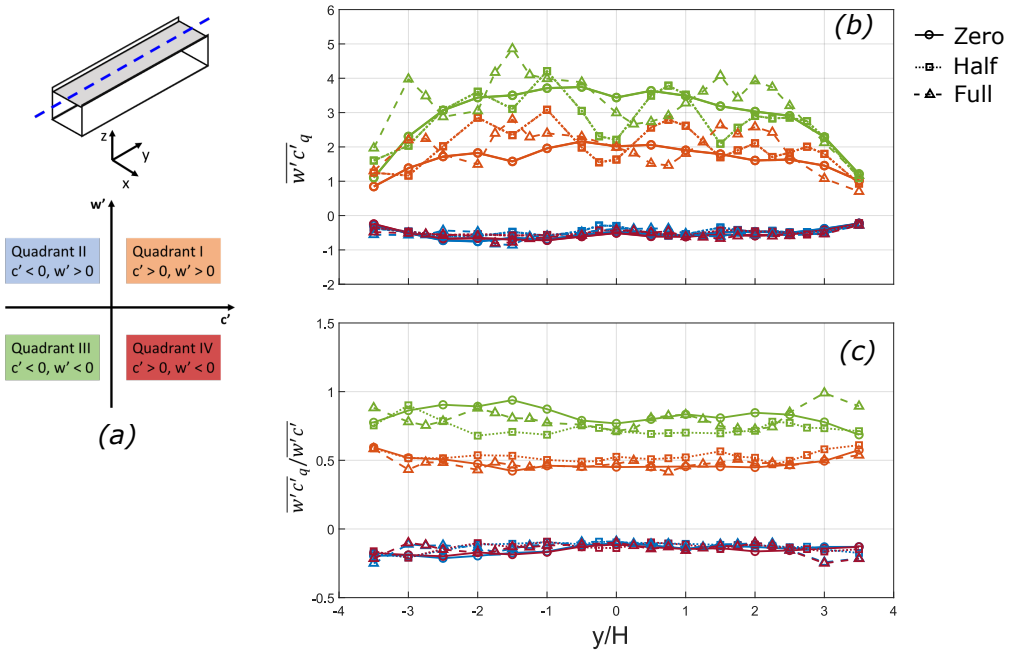

Figure 14: Quadrant analysis of $\overline{w'c'}$ at the rooftop of the canyon ($x/H = 1$, $z/H = 0.98$). (a) Schematic representation of the quadrants in the plane $\{c', w'\}$. (b) Local quadrant contributions to $\overline{w'c'}$. (c) Normalized quadrant contributions to $\overline{w'c'}$. The blue dotted line on the shaded plane in the bottom inset represents the position where the quadrant analysis was performed.

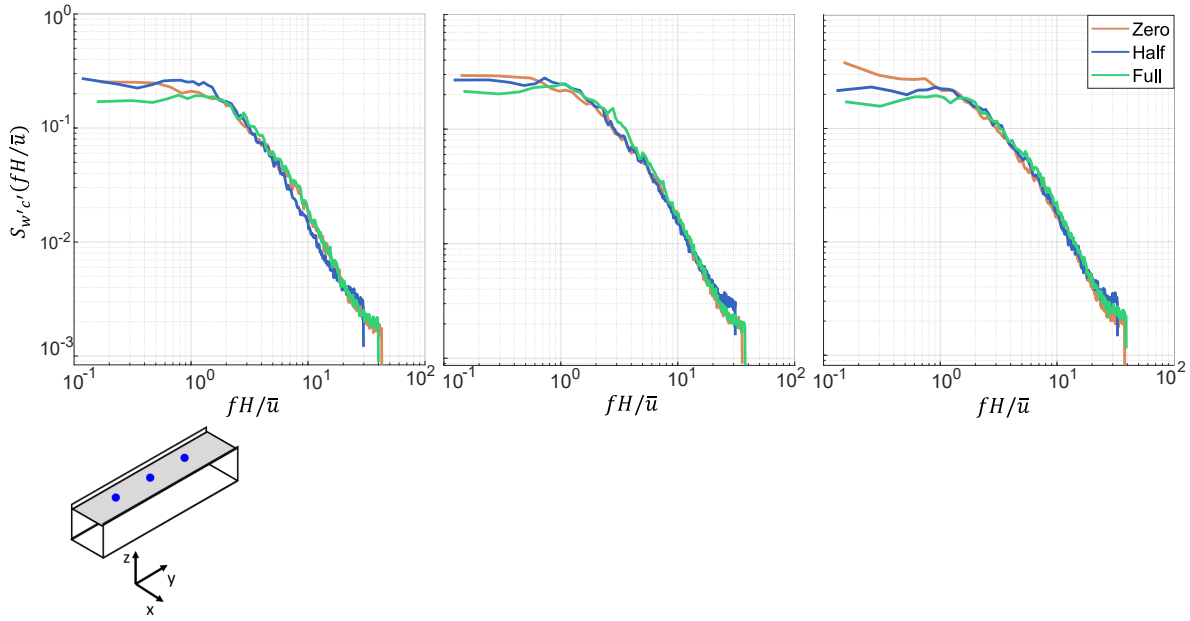

Figure 15: Spectra of $w'c'(t)$ calculated in three different sampling points along the central line (x/H=1) at the rooftop (z/H=0.98): (a) y/H=-1.5, (b) y/H=0, (c) y/H=2. The blue points on the shaded plane in the bottom inset represent the positions where the spectra were calculated.

(panel b2), while they uniformly approach zero in the Full configuration (panel b3). This reveals that $\overline{w'c'}^*$ is inhibited by an increasing tree density. Regardless of the presence of trees, $\overline{w'c'}^*$ at the interface between the canyon and the external flow (notably z/H=0.98) sharply increases to the same value (around 8), in line with σ_w^* and k^* (Fig. 4, panels b1-b3 and c1-c3, respectively). The total mass fluxes (4c1-c3) have the same spatial distribution of the advective fluxes, with lower tree density leading to higher heterogeneity along the y-axis. In the Zero and Half configurations, the contribution of the negative turbulent fluxes enhances the downward fluxes (blue areas in panels c1 and c2).

The mean mass flux and the mean vertical velocity (Fig. 13a1-a3 and Fig. 5a1-a3, respectively) follow the same behavior at the rooftop as well. In the non-vegetated canyon (panel a1 of Fig. 13), the mean flux is homogeneous and negative along the downwind wall (x/H=1.5), where the external flow (without pollutant) enters the canyon, and homogeneous and positive along the upwind wall (x/H=0.5), where the polluted air leaves the canyon. We detect the same streamwise pattern in the vegetated canyons (panels a2, a3), but the outgoing mean flux is broken into smaller flux segments by the presence of trees. Moreover, positive $\bar{w}^*\bar{c}^*$ fluxes are weaker in the Half configuration (panel a2), while their intensity is not homogeneous along y in the Full configuration (panel a3). Turbulent mass fluxes (panels b1-b3) are positive and quite homogeneous in all configurations with significantly larger values than inside the canyon (Marucci and Carpentieri, 2019), especially in the presence of trees (panels b2, b3). As already observed inside the canyon, the total vertical mass fluxes (panels c1-c3) follow the same trend of $\bar{w}^*\bar{c}^*$, but the strong positive contribution of the turbulent fluxes enhances the upward transport, and leads to slightly positive fluxes at the downwind wall. Therefore, the upward total mass fluxes at the upwind wall are significantly higher than the mean ones, and they are more heterogeneous with the increase in tree density.

In order to understand if the positive turbulent mass fluxes detected at the rooftop (Fig. 13b1-b3) are due to the entrance of clean external flow or to the leaving of polluted air from the canyon, we perform the quadrant analysis (e.g. Di Bernardino et al., 2018). The time series of $w'c'(t)$ are decomposed on the four quadrants of the Cartesian plane $\{c',w'\}$. In Fig. 14a, we report a scheme of the quadrant division: quadrant I identifies outflow events with a concentration higher than the mean, while quadrant III inflow events with a concentration lower than the mean.

In Fig. 14b, we report for a longitudinal profile at the centre of the canyon rooftop ($x/H = 1$ and $z/H = 0.98$) the local contribution of each quadrant, defined as the sum of the turbulent fluxes in the quadrant ($\overline{w'c'_q}$, where q=I, II, III, IV). Regardless of the presence of trees, the contributions of quadrants II and IV, which represent negative turbulent mass fluxes, are negligible relative to the ones of quadrants I and III, as expected (see Fig. 13b1-b3). The contribution of quadrant III is

higher than the one of quadrant I, meaning that the entrance of external clean air provides an higher contribution to the positive turbulent mass fluxes in the centre of the canyon rooftop than the exiting of polluted air. Comparing the different tree density configurations, we notice a clear distinction between the spatial homogeneity of the profiles of quadrant I and III in the Zero configuration (continuous lines), and their heterogeneity in the vegetated canyons (dashed lines). Thus, the presence of trees affects the local contribution of inflow and outflow events. Conversely, the normalized quadrant contributions to $\overline{w'c'}$ – expressed as the ratio between $\overline{w'c'_q}$ and the total contribution of all quadrants ($\overline{w'c'}$) – is uniform along the canyon axis, regardless of the presence of trees (Fig. 14c).

We performed the spectral analysis of $w'c'(t)$ signal, to investigate the turbulent scales involved in the turbulent mass transport at the rooftop of the canyon. Figure 15 shows the spectra of the normalized mass fluxes $(w'c'(t)-\overline{w'c'})/\sigma_{w'c'}$ (where $\sigma_{w'c'}$ is the standard deviation of $w'c'(t)$ signal), calculated at $y/H = [-1.5, 0, 2]$, along the central profile at the canyon rooftop. As we observed in the vertical velocity spectra (Fig. 6), the large-scale structures dominate the turbulent mass transport in the empty canyon, and the energy associated to them decreases with the increase in tree density.

5 Conclusion

The aim of the present study was to investigate the impact of tree-lined avenues on turbulent flow and concentration fields, and on the vertical mass transport in an urban street canyon, subject to an external boundary layer. This was addressed by performing concentration, velocity, and combined concentration-velocity measurements inside a large canyon (H/W_c=0.5) oriented perpendicular to the wind direction, in a wind tunnel. Three different tree densities were considered: an empty canyon (Zero configuration), a canyon with low tree density (Half configuration), and a canyon with high tree density (Full configuration).

The increase of vegetation density leads to a partial homogenization of the mean vertical velocity field and to a reduction of the turbulent kinetic energy, inside the canyon. However, at the rooftop, the presence of trees does not significantly smooth the intensity of velocity fluctuations, but, it partially hinders the mean vertical velocity at the upwind wall. The tree-induced reduction of turbulent fluctuations unveils a peculiar effect of high-density vegetation on turbulent dynamics inside a canyon. This effect deserves the attention of the scientific community as tree avenues with intersecting crowns are common in many European cities.

Concerning concentration fluctuations, we found that vegetation induces a transition from an almost homogeneous pattern (characteristic of the non-vegetated canyon), to a heterogeneous one, both inside the canyon and at the rooftop. On

average, the intensity of concentration fluctuations is not significantly smoothed by the presence of trees, rather local maxima are exacerbated in the vegetated canyons than in the empty one. The coefficient of variation of the concentration does not show a significant spatial pattern with the tree density, even if we notice that it slightly decreases in the Full configuration. Within the canyon, the C_v assumes values that vary between 0.4 and 0.6.

The statistical analysis of the concentration time series reveals that the concentration pdf is skewed towards positive values, it has fatter tails with respect to the Gaussian distribution, and it maintains the same shape in the different tree density configurations. The gamma and the lognormal distributions perform a good fitting of the experimental pdf in the Zero and Half configurations, while in the Full configuration, the lognormal distribution is the best model. In all configurations, the lognormal distribution provides the best estimate of the third and fourth moments.

The total mass fluxes are mainly governed by the mean mass fluxes, which in turn show almost the same pattern of the mean vertical velocity. The pattern of mean mass fluxes depends on vegetation: inside the canyon, the mean mass fluxes show a well-organized spatial pattern in the empty canyon, which is lost increasing the tree density and, at the rooftop, the upward mean mass fluxes are hindered by trees. Turbulent mass fluxes are homogeneous and negative inside the non-vegetated canyon, while they are reduced to almost zero with high vegetation density. The vegetation-induced decrease in the turbulent mass fluxes (as well as vertical velocity standard deviation and turbulent kinetic energy) may be responsible for a reduction of the mixing inside the canyon, leading to a more heterogeneous scalar field in the vegetated canyon. At the rooftop, turbulent fluxes are high and positive and their intensity is not affected by the presence of trees. The quadrant analysis reveals that, regardless of the presence of trees, the inflow events of clean air (quadrant III) provides an higher contribution to the positive turbulent mass fluxes at the rooftop than outflow events of polluted air (quadrant I). Moreover, we showed that the normalized contribution of inflow and outflow events to $\overline{w'c'}$ is homogeneous along the longitudinal direction of the canyon. On the contrary, in the presence of trees, the local contribution of outflow (quadrant I) and inflow events is heterogenous along the longitudinal axis of the rooftop.

The spectral analysis of the vertical velocity and turbulent mass fluxes signals revealed that the energy content of large-scale structures decreases with the increase in tree density, or rather the decrease in tree spacing.

The wind-tunnel experimental campaign allowed us to highlight the complexity of the turbulent mass transport within an urban street canyon, with different vegetation densities. While high vegetation density has been shown to enhance thermal comfort and urban biodiversity, its impact on air quality remains a subject of debate. On one hand tree avenues increase pollutant deposition and regulate local temperature; on the other hand the tree crowns, especially the intersecting ones,

hinder the vertical mean flow and dampen turbulent kinetic energy and turbulent mass fluxes. As a consequence of that, at the pedestrian level, the transport and the mixing is less efficient, mostly close to the upwind wall, an issue which has to be considered together with the beneficial effects of high tree density.

A limit of the present study was that the experimental equipment employed to measure velocity and mass fluxes (LDA, mirror, LDA-FID system) was not suitable to perform measurements close to the canyon walls, due to the reflection of the laser beams on the miniatures of trees. This issue prevented us to capture the three-dimensionality of the turbulent flow and scalar transport within the canyon, thus to completely identify the flow dynamics leading to the formation of concentration peaks in a vegetated canyon. However, we provided high-resolution measurements of the mean and turbulent concentration, vertical flow velocity, and mass fluxes in the centre and at the rooftop of the canyon, together with an estimate of aerodynamic porosity and drag coefficient of the model trees. These measurements are useful to validate numerical models, aimed at simulating flow and dispersion in urban-like geometries in presence of vegetation. Moreover, a new experimental campaign is currently underway to investigate the effect of vegetation on the flow field considering different orientations of the canyon with respect to the external flow.

Data availability

The experimental dataset is available on the website:
https://doi.org/10.5281/zenodo.7757044 (Fellini et al., 2023). We provide concentration, velocity, and turbulent mass fluxes data within the canyon, and the characterization of the flow field above the buildings.

References

Abhijith K, Kumar P, Gallagher J, McNabola A, Baldauf R, Pilla F, Broderick B, Di Sabatino S, Pulvirenti B (2017) Air pollution abatement performances of green infrastructure in open road and built-up street canyon environments – A review. Atmospheric Environment 162:71–86

Allegrini J, Dorer V, Carmeliet J (2013) Wind tunnel measurements of buoyant flows in street canyons. Building and Environment 59:315–326

Armson D, Stringer P, Ennos AR (2013) The effect of street trees and amenity grass on urban surface water runoff in Manchester, UK. Urban Forestry & Urban Greening 12(3):282–286

Blackman K, Perret L, Savory E (2015) Effect of upstream flow regime on street canyon flow mean turbulence statistics. Environmental Fluid Mechanics 15(4):823–849

Blackman K, Perret L, Savory E (2018) Effects of the upstream-flow regime and canyon aspect ratio on non-linear interactions between a street-canyon flow and the overlying boundary layer. Boundary-Layer Meteorology 169:537–558

Buccolieri R, Gromke C, Di Sabatino S, Ruck B (2009) Aerodynamic effects of trees on pollutant concentration in street canyons. Science of the Total Environment 407(19):5247–5256

Cassiani M, Bertagni MB, Marro M, Salizzoni P (2020) Concentration fluctuations from localized atmospheric releases. Boundary-Layer Meteorology 177:461–510

Di Bernardino A, Monti P, Leuzzi G, Querzoli G (2015) Water-channel study of flow and turbulence past a two-dimensional array of obstacles. Boundary-Layer Meteorology 155(1):73–85

Di Bernardino A, Monti P, Leuzzi G, Querzoli G (2018) Pollutant fluxes in two-dimensional street canyons. Urban climate 24:80–93

Diener A, Mudu P (2021) How can vegetation protect us from air pollution? A critical review on green spaces' mitigation abilities for air-borne particles from a public health perspective – with implications for urban planning. Science of the Total Environment 796:148,605

Fellini S, Ridolfi L, Salizzoni P (2020) Street canyon ventilation: Combined effect of cross-section geometry and wall heating. Quarterly Journal of the Royal Meteorological Society 146(730):2347–2367

Fellini S, Marro M, Del Ponte AV, Barulli M, Soulhac L, Ridolfi L, Salizzoni P (2022) High resolution wind-tunnel investigation about the effect of street trees on pollutant concentration and street canyon ventilation. Building and Environment 226:109,763

Fellini S, Del Ponte AV, Marro M, Salizzoni P (2023) Wind tunnel measurements of concentration and velocity in urban geometries with trees. DOI 10.5281/zenodo.7757044

Ferrini F, Fini A (2011) Sustainable management techniques for trees in the urban areas. Journal of Biodiversity and ecological sciences 1(1):1–20

Ferrini F, Fini A, Mori J, Gori A (2020) Role of vegetation as a mitigating factor in the urban context. Sustainability 12(10):4247

Finn D, Clawson KL, Carter RG, Rich JD, Biltoft C, Leach M (2010) Analysis of urban atmosphere plume concentration fluctuations. Boundary-layer meteorology 136:431–456

Finnigan J (2000) Turbulence in plant canopies. Annual review of fluid mechanics 32(1):519–571

Fischer HB, List JE, Koh CR, Imberger J, Brooks NH (1979) Mixing in inland and coastal waters. Accademic Press

Garbero V, Salizzoni P, Soulhac L (2010) Experimental study of pollutant dispersion within a network of streets. Boundary-layer meteorology 136:457–487

Grilo F, Pinho P, Aleixo C, Catita C, Silva P, Lopes N, Freitas C, Santos-Reis M, McPhearson T, Branquinho C (2020) Using green to cool the grey: Modelling the cooling effect of green spaces with a high spatial resolution. Science of the Total Environment 724:138,182

Gromke C, Ruck B (2007) Influence of trees on the dispersion of pollutants in an urban street canyon – experimental investigation of the flow and concentration field. Atmospheric Environment 41(16):3287–3302

Gromke C, Ruck B (2009) On the impact of trees on dispersion processes of traffic emissions in street canyons. Boundary-Layer Meteorology 131(1):19–34

Gromke C, Ruck B (2012) Pollutant concentrations in street canyons of different aspect ratio with avenues of trees for various wind directions. Boundary-Layer Meteorology 144(1):41–64

Gromke C, Buccolieri R, Di Sabatino S, Ruck B (2008) Dispersion study in a street canyon with tree planting by means of wind tunnel and numerical investigations – evaluation of CFD data with experimental data. Atmospheric Environment 42(37):8640 – 8650

Grylls T, van Reeuwijk M (2021) Tree model with drag, transpiration, shading and deposition: Identification of cooling regimes and large-eddy simulation. Agricultural and Forest Meteorology 298:108,288

Grylls T, van Reeuwijk M (2022) How trees affect urban air quality: It depends on the source. Atmospheric Environment 290:119,275

Hewitt CN, Ashworth K, MacKenzie AR (2020) Using green infrastructure to improve urban air quality (GI4AQ). Ambio 49:62–73

Jaroslawski T, Savory E, Perret L (2020) Roof-level large-and small-scale coherent structures in a street canyon flow. Environmental Fluid Mechanics 20:739–763

Kaimal JC, Wyngaard J, Izumi Y, Coté O (1972) Spectral characteristics of surface-layer turbulence. Quarterly Journal of the Royal Meteorological Society 98(417):563–589

Kukačka L, Nosek Š, Kellnerová R, Jurčáková K, Jaňour Z (2012) Wind tunnel measurement of turbulent and advective scalar fluxes: a case study on intersection ventilation. The Scientific World Journal 2012:1–13

Li J, Bilger R (1996) The diffusion of conserved and reactive scalars behind line sources in homogeneous turbulence. Journal of Fluid Mechanics 318:339–372

Manickathan L, Defraeye T, Allegrini J, Derome D, Carmeliet J (2018) Comparative study of flow field and drag coefficient of model and small natural trees in a wind tunnel. Urban Forestry & Urban Greening 35:230–239

Marro M, Gamel H, Méjean P, Correia H, Soulhac L, Salizzoni P (2020) High-frequency simultaneous measurements of velocity and concentration within turbulent flows in wind-tunnel experiments. Experiments in Fluids 61(12):1–13

Marucci D, Carpentieri M (2019) Effect of local and upwind stratification on flow and dispersion inside and above a bi-dimensional street canyon. Building and Environment 156:74–88

Merlier L, Jacob J, Sagaut P (2018) Lattice-Boltzmann Large-Eddy Simulation of pollutant dispersion in street canyons including tree planting effects. Atmospheric Environment 195:89–103

Moonen P, Gromke C, Dorer V (2013) Performance assessment of large eddy simulation (LES) for modeling dispersion in an urban street canyon with tree planting. Atmospheric environment 75:66–76

Neophytou MA, Markides C, Fokaides P (2014) An experimental study of the flow through and over two-dimensional rectangular roughness elements: Deductions for urban boundary layer parameterizations and exchange processes. Physics of Fluids 26(8):086,603

Nironi C, Salizzoni P, Marro M, Mejean P, Grosjean N, Soulhac L (2015) Dispersion of a passive scalar fluctuating plume in a turbulent boundary layer. Part I: Velocity and concentration measurements. Boundary-layer meteorology 156(3):415–446

Nowak DJ, Crane DE (2002) Carbon storage and sequestration by urban trees in the USA. Environmental pollution 116(3):381–389

Oettl D, Ferrero E (2017) A simple model to assess odour hours for regulatory purposes. Atmospheric environment 155:162–173

Oliveira S, Andrade H, Vaz T (2011) The cooling effect of green spaces as a contribution to the mitigation of urban heat: A case study in Lisbon. Building and environment 46(11):2186–2194

Orsi M, Soulhac L, Feraco F, Marro M, Rosenberg D, Marino R, Boffadossi M, Salizzoni P (2021) Scalar mixing in homogeneous isotropic turbulence: A numerical study. Physical Review Fluids 6(3):034,502

Perret L, Basley J, Mathis R, Piquet T (2019) The atmospheric boundary layer over urban-like terrain: influence of the plan density on roughness sublayer dynamics. Boundary-Layer Meteorology 170:205–234

Pietri L, Petroff A, Amielh M, Anselmet F (2009) Turbulence characteristics within sparse and dense canopies. Environmental fluid mechanics 9(3):297–320

Poggi D, Katul G (2007a) Turbulent flows on forested hilly terrain: the recirculation region. Quarterly Journal of the Royal Meteorological Society: A journal of the atmospheric sciences, applied meteorology and physical oceanography 133(625):1027–1039

Poggi D, Katul GG (2007b) An experimental investigation of the mean momentum budget inside dense canopies on narrow gentle hilly terrain. Agricultural and forest meteorology 144(1-2):1–13

Poggi D, Porporato A, Ridolfi L, Albertson J, Katul G (2004) The effect of vegetation density on canopy sub-layer turbulence. Boundary-Layer Meteorology 111:565–587

Poggi D, Katul G, Albertson J (2006) Scalar dispersion within a model canopy: Measurements and three-dimensional lagrangian models. Advances in Water Resources 29(2):326–335

Raupach M, Coppin P, Legg B (1986) Experiments on scalar dispersion within a model plant canopy part i: The turbulence structure. Boundary-Layer Meteorology 35:21–52

Raupach MR, Antonia RA, Rajagopalan S (1991) Rough-wall turbulent boundary layers. Applied Mechanics Reviews 44(1):1–25

Raupach MR, Finnigan JJ, Brunet Y (1996) Coherent eddies and turbulence in vegetation canopies: the mixing-layer analogy. Boundary-Layer Meteorology 25th Anniversary Volume, 1970–1995: Invited Reviews and Selected Contributions to Recognise Ted Munn's Contribution as Editor over the Past 25 Years pp 351–382

Salizzoni P, Soulhac L, Mejean P, Perkins RJ (2008) Influence of a two-scale surface roughness on a neutral turbulent boundary layer. Boundary-layer meteorology 127(1):97–110

Salizzoni P, Soulhac L, Mejean P (2009) Street canyon ventilation and atmospheric turbulence. Atmospheric Environment 43(32):5056–5067

Salizzoni P, Marro M, Soulhac L, Grosjean N, Perkins RJ (2011) Turbulent transfer between street canyons and the overlying atmospheric boundary layer. Boundary-layer meteorology 141(3):393–414

Sawford B, Stapountzis H (1986) Concentration fluctuations according to fluctuating plume models in one and two dimensions. Boundary-layer meteorology 37(1-2):89–105

Stapountzis H, Sawford B, Hunt J, Britter R (1986) Structure of the temperature field downwind of a line source in grid turbulence. Journal of Fluid Mechanics 165:401–424

Van Renterghem T, Forssén J, Attenborough K, Jean P, Defrance J, Hornikx M, Kang J (2015) Using natural means to reduce surface transport noise during propagation outdoors. Applied Acoustics 92:86–101

Yassin M (2008) Probability characteristics of concentration fluctuations in plume dispersal. Journal of Engineering Sciences 36(1):115–130

Zhao Y, Chew LW, Fan Y, Gromke C, Hang J, Yu Y, Ricci A, Zhang Y, Xue Y, Fellini S, et al. (2023) Fluid Tunnel Research for Challenges of Urban Climate. arXiv preprint arXiv:230103001

Zölch T, Henze L, Keilholz P, Pauleit S (2017) Regulating urban surface runoff through nature-based solutions – an assessment at the micro-scale. Environmental research 157:135–144
1

Appendix 1: Expressions of the third and fourth moments of the gamma, lognormal and Weibull distributions

The skewness and kurtosis of the gamma, lognormal and Weibull 2p distributions are reported as a function of the only parameter C_v:

1. gamma distribution:

$$\begin{aligned} S_k(\vartheta) &= \frac{2}{\sqrt{\vartheta}} \\ K_u(\vartheta) &= \frac{6}{\vartheta} + 3 \end{aligned} \tag{8}$$

   where ϑ is defined as $\vartheta = C_v^{-2}$.

2. lognormal distribution:

$$\begin{aligned} S_k(C_v) &= [\exp(\ln(1 + C_v) + 2]\sqrt{\exp[\ln(1 + C_v^2)] - 1} \\ K_u(C_v) &= \exp[4\ln(1 + C_v^2)] + 2\exp[3\ln(1 + C_v^2)] + 3\exp[2\ln(1 + C_v^2)] - 3 \end{aligned} \tag{9}$$

3. Weibull 2p distribution:

$$\begin{aligned} S_k(C_v) &= \Gamma\left(1 + \frac{3}{C_v^{-1.086}}\right)C_v^{-3}a_w^3 - 3C_v^{-1} - C_v^{-3} \\ K_u(C_v) &= \Gamma\left(1 + \frac{4}{C_v^{-1.086}}\right)C_v^{-4}a_w^4 - 4S_kC_v^{-1} - 6C_v^{-2} - C_v^{-4}. \end{aligned} \tag{10}$$

   where

$$a_w = \frac{1}{\Gamma(1 + C_v^{1.086})} \tag{11}$$